Phase Diagram for Nanostructuring CaF_2 Surfaces by Slow Highly Charged Ions

A. S. El-Said*
Institute of Ion Beam Physics and Materials Research, Helmholtz-Zentrum Dresden-Rossendorf, 01328 Dresden, Germany, EU; Physics Department, Faculty of Science, Mansoura University, 35516 Mansoura, Egypt

R. A. Wilhelm, R. Heller, and S. Facsko†
Institute of Ion Beam Physics and Materials Research, Helmholtz-Zentrum Dresden-Rossendorf, 01328 Dresden, Germany, EU

C. Lemell, G. Wachter, and J. Burgdörfer
Institute for Theoretical Physics, Vienna University of Technology, Wiedner Hauptstr. 8-10, A-1040 Vienna, Austria, EU

R. Ritter and F. Aumayr‡
Institute of Applied Physics, TU Wien-Vienna University of Technology, 1040 Vienna, Austria, EU
(Received 24 February 2012; published 14 September 2012)

The impact of individual slow highly charged ions (HCI) on alkaline earth halide and alkali halide surfaces creates nano-scale surface modifications. For different materials and impact energies a wide variety of topographic alterations have been observed, ranging from regularly shaped pits to nano-hillocks. We present experimental evidence for the creation of thermodynamically stable defect agglomerations initially hidden after irradiation but becoming visible as pits upon subsequent etching. A well defined threshold separating regions with and without etch-pit formation is found as a function of potential and kinetic energies of the projectile. Combining this novel type of surface defects with the previously identified hillock formation, a phase diagram for HCI induced surface restructuring emerges. The simulation of the energy deposition by the HCI in the crystal provides insight into the early stages of the dynamics of the surface modification and its dependence on the kinetic and potential energies.

DOI: 10.1103/PhysRevLett.109.117602 PACS numbers: 79.20.Rf, 34.35.+a, 61.80.Jh

Studies of the interactions of slow ($v < v_{\mathrm{Bohr}}$), highly charged ions (HCIs) with solid surfaces were originally aimed at gaining an understanding of the dynamical processes governing neutralization, relaxation, and eventual dissipation of the very high potential energy density ($\sim$ keV/Å^3) within a few femtoseconds ([1] and references therein). This potential energy carried into the collision is given by the sum of binding energies of all missing electrons. More recently, the focus has shifted to material-science driven applications, specifically to the development of novel techniques for material modification [2–5] and improved surface analysis [6,7]. Various types of surface nanostructures such as nanosized hillocks, pits or craters have so far been observed after the impact of individual HCI on different materials [8–11]. Their topography, appearance, and long-time stability seem to depend sensitively on the material properties as well as on the potential energy (charge state) and kinetic energy of the incident ion (for a recent review see Ref. [12]).

Surprisingly, even for very similar prototypical wide-band-gap insulators, ionic crystals of alkali halides and alkaline earth halides, vastly different and seemingly contradictory results have been found. Irradiation of KBr single crystals by individual highly charged Xe ions leads to the formation of pits of one atomic layer depth [11] while irradiation of CaF_2 single crystals produces nanometer high hillocks protruding from the surface [8]. In both cases the surface nanostructures were shown to be the result of individual ion impacts; i.e., every structure is caused by the impact of a single ion and a threshold value for the potential energy of the projectile has to be surpassed before the nanostructure can be observed. However, while for KBr this threshold potential energy for pit formation strongly decreases with increasing kinetic energy of the HCI [11], for hillock formation in CaF_2 only a slight yet noticeable increase with increasing kinetic energy is observed [8].

In this Letter we present experimental evidence which supplies the missing pieces to this puzzle and allows us to construct a phase diagram as a function of kinetic and potential energies for the formation of different nanosized defect structures in CaF_2. In addition, simulation of the early stages of dissipation of the energy deposited by the HCIs reveals characteristic differences in the relaxation dynamics as a function of potential and kinetic energies which can be considered to be the precursors of the eventual formation of different stable surface structures. The key is the search for previously unobserved "hidden" surface structures after irradiation by ions with potential energies below the threshold for nano-hillock formation. By etching the samples we discover a second threshold at lower potential energy above which CaF_2 undergoes a nanoscale structural transformation even though it is not evident as a topographic change. It becomes, however,

visible in the form of triangular pits after chemical etching. This threshold depends on both the potential and the kinetic energies of the HCIs closely resembling the threshold behavior found for pit formation on KBr. Accompanying molecular dynamics simulations suggest this second threshold to be associated with lattice defect aggregation in CaF_2 following electronic excitations caused by the HCI-surface interaction.

Thin platelets of CaF_2 were prepared by cleaving a high purity single-crystal block grown from melt in an inert atmosphere along the (111) plane. This cleavage is known to produce atomically flat fluorine-terminated surfaces which are ideal for observing surface topographic changes down to the nanometer scale [13]. $^{129}Xe^{q+}$ ions were extracted from the electron beam ion trap at the Two-Source-Facility of the Helmholtz-Zentrum Dresden-Rossendorf using an electrostatic potential of 4.5 kV. By using a two stage deceleration system and adjusting the potential difference between source and target from 4.5 kV down to 0.18 kV, highly charged Xe^{q+} projectiles over a wide range of charge states ($10 \leq q \leq 33$, corresponding to potential energies of 0.8 keV $\leq E_{pot} \leq$ 21.2 keV) and kinetic impact energies (6 keV $\leq E_{kin} \leq$ 150 keV) could be produced. The applied ion fluences were chosen between 0.5 and 5×10^8 ions/cm^2, small enough to avoid overlapping of impact sites and high enough to obtain reasonable statistics. The time averaged current density varied between $\sim 10^4$ and $\sim 3 \times 10^5$ ions/s/cm^2 as derived from the ion count rate and a circular beam spot with a diameter of 6 mm. The surfaces of the irradiated samples were investigated using atomic force microscopy (AFM) (Veeco Multimode). The AFM was operated in contact mode with a constant loading force of less than 5 nN using nonconductive Si_3N_4 sensors (Veeco Instruments) with cantilevers of force constants ~ 0.1 Nm. The image processing was performed using the WSXM software [14]. Ion-irradiated CaF_2 samples were chemically etched using a HNO_3 solution (10% vol.) at room temperature without agitation [13]. Each platelet was immersed once in the etchant, subsequently in deionized water, and was finally dried in a stream of dry nitrogen. It should be emphasized that we use much shorter etching times t_e than applied in standard etching techniques. For the latter, typically $t_e \gtrsim 1$ minute yields etch pits even starting from randomly occurring atomic-scale dislocations and much of the sensitivity to hidden defect aggregates would be lost. Due to the dramatically enhanced etching speed in regions with a high defect density caused by the HCIs (~ 20 nm/s compared to a regular lateral etching speed of less than 3 nm/s [13]), $t_e =$ 10 s turned out to be the optimum etching time combining good visibility of etch pits in AFM while selecting only defect clusters created by HCI impact. The presented structures with dimensions in the range of a few 100 nm in lateral and vertical direction are by far larger than the topographic resolution of the ambient AFM in contact mode.

The observation of a pattern of well-defined irradiated and masked areas (Fig. 1) for 150 keV Xe^{33+} ion impact on

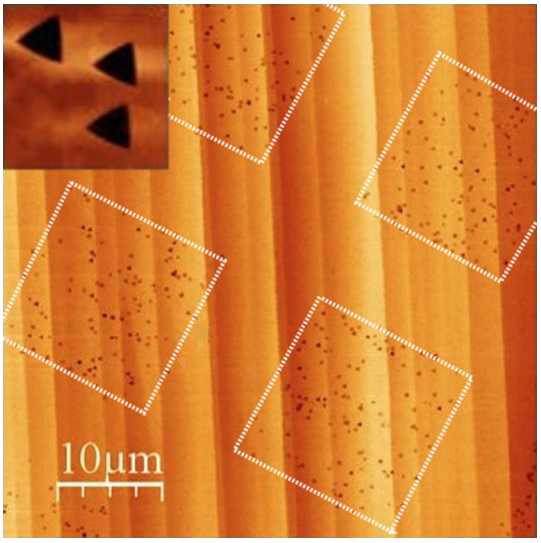

FIG. 1 (color online). AFM topographic image (50×50 μm^2) of a CaF_2 surface showing etch pits after exposure to 150 keV Xe^{33+} ions. The sample was irradiated through a mask (indicated by dotted lines) and subsequently chemically etched using HNO_3. The inset in the upper left corner shows a magnification of the etch pits (1.5×1.5 μm^2).

CaF_2 (111) is direct evidence of HCI induced surface defects which can be clearly distinguished from randomly occurring dislocations and surface damage. In irradiated areas, etch pits of regularly structured 3-faced symmetric triangular depressions appear which are similar to those observed after irradiation and etching of BaF_2 [15]. This particular geometrical shape originates from the (111) crystal lattice orientation of the CaF_2 sample [13]. The number of pits is in good agreement with the applied ion fluence; i.e., each etch pit is created by a single ion impact. We suppose the pits are localized at the sites where HCI impact created hillocks were situated prior to etching. The charge state ($q = 33$) of the incident ion corresponds to a potential energy well above the threshold for nanohillock formation.

Lowering the charge state to values below the potential energy threshold for hillock formation ($q_{th} \approx 28$ for Xe; $E_{pot} = 12$ keV) reveals the appearance of similar pits in the absence of preceding hillocks (Fig. 2). At the same kinetic energy of $E_{kin} = 40$ keV for "low" charge states ($q \lesssim 18$) no damage of the etched surface is visible, whereas at a higher charge state ($q = 25$, $E_{pot} = 8.1$ keV) etch pits appear.

In order to investigate the influence of both potential and kinetic energies on etch pit formation, we performed systematic irradiations with $^{129}Xe^{q+}$ projectiles of different charge states ($q = 10$ to 33) and with varying kinetic energy on CaF_2. The resulting thermodynamically stable damage structures and modifications can be summarized by a "phase diagram" with potential and kinetic energies as state variables (Fig. 3). Three different phases pertaining to surface

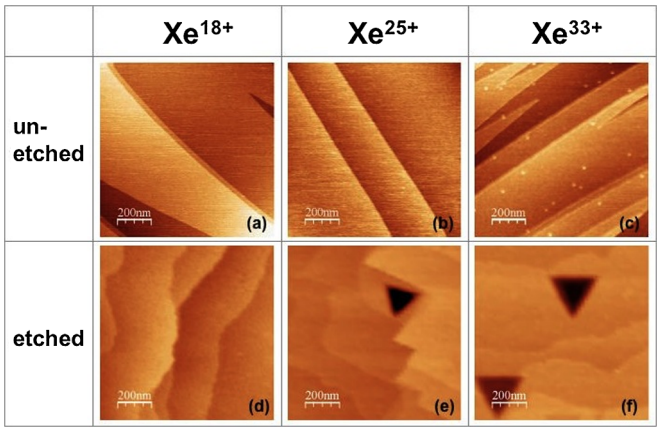

FIG. 2 (color online). Topographic contact-mode AFM images of CaF_2 (111) samples irradiated by 40 keV Xe ions in different charge states (columns): (a), (d) Xe^{18+}, (b), (e) Xe^{25+}, and (c), (f) Xe^{33+}. In each frame an area of 1 μm × 1 μm is displayed. Upper row: resulting images without etching (a), (b), (c). Lower row: images after etching by HNO_3 (d), (e), (f). Ion fluences were 2×10^8 ions/cm^2 for (e), (f) and 1–2 × 10^9 ions/cm^2 for (a), (b), (c), (d).

restructuring can be distinguished: the stability region *A* without detectable surface modification after HCI impact [Figs. 2(a) and 2(d)], region *B* in which defect clusters become visible as regularly shaped pits only upon etching [Figs. 2(b) and 2(e)], and the nanohillock region *C* [Figs. 2(c) and 2(f)] in which hillocks resulting from nanomelting can be observed after irradiation. The nanomelting arises from the transfer of high local energy density during HCI impact and is followed by a rapid quenching resulting in the formation of a hillock-like structure (nanohillock) [8]. Pits appear in phase *C* only after etching presumably at the

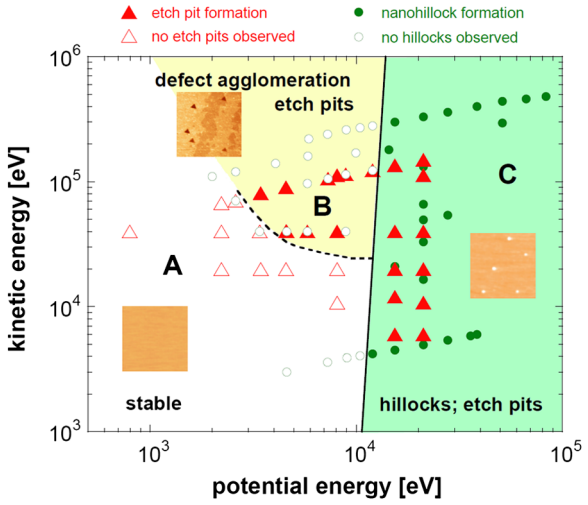

FIG. 3 (color online). Hillock and etch pit formation on CaF_2 (111) induced by irradiation with highly charged Xe ions. Full (open) green circles show pairs of potential and kinetic energies where hillocks are produced (absent) after irradiation, full (open) red triangles indicate pairs where pits are present (missing) after etching the irradiated samples.

positions of the hillocks which could not be found on the etched surface.

While the threshold for hillock formation strongly depends on potential energy but only weakly on kinetic energy [8,12] implying an almost vertical boundary of region *C* in Fig. 3, the border separating the stability region *A* and the defect agglomeration region *B* (etch pits) is strongly dependent on both kinetic and potential energies. Ions with lower kinetic energy require more potential energy to create etchable damage than faster ones. Such synergistic effects of kinetic and potential energies have previously been observed for pit formation in KBr [11], however, with the difference that no chemical etching was a prerequisite for the pits to be observed. This may be related to the much higher defect mobility in KBr than in CaF_2 leading to a more efficient transport of defects to the surface immediately followed by material desorption.

These experimental findings suggest a scenario for nanostructure formation on alkaline earth halides and alkali halides involving initial heating of electrons by multiple electron transfer and Auger relaxation, hot electron transport and dissipation with accompanying lattice heating by electron-optical phonon coupling, and finally atomic motion in the heated crystal which results in dislocations, defects, and structural weakening of the cooled lattice. The early stages of defect formation can be simulated within a three-step model exploiting disparate time scales of the underlying processes: the initial electronic energy deposition of the HCIs occurring on the (sub) femtosecond time scale can be described by the classical-over-barrier model [16], the hot electron transport and lattice heating occurring on a sub-picosecond time scale by classical electron-transport simulations [17], and finally the atomic motion by a molecular-dynamics (MD) simulation which we follow for up to 15 ps [18]. It should be noted that accurate potential surfaces for ionic crystals, in particular, in the presence of excitations and charge transfer entering the MD simulation, are not available. Following the system on longer time scales and reaching the regime of formation of thermodynamically stable phases is, thus, not possible. Our simulation results can therefore provide only qualitative, yet important, insights into the early stages of defect formation and aggregation. The following qualitative trends can be readily extracted. For HCIs in "low" charge states (Fig. 4, left) only a few (i.e., low density) individual defects (point defects, single vacancies) are created at or below the surface, where we take the distance individual fluorine atoms travel during ~15 ps as measure for the eventual defect formation probability. These defects either remain below the surface, easily anneal or are too small to be detected by means of AFM. Since the etchability of CaF_2 is strongly coupled to the creation of large defect aggregates [19] rather than to point defects, no pits are observed after etching. Our MD simulations do not yield any significant number of lattice displacements for low q (well below ~1%).

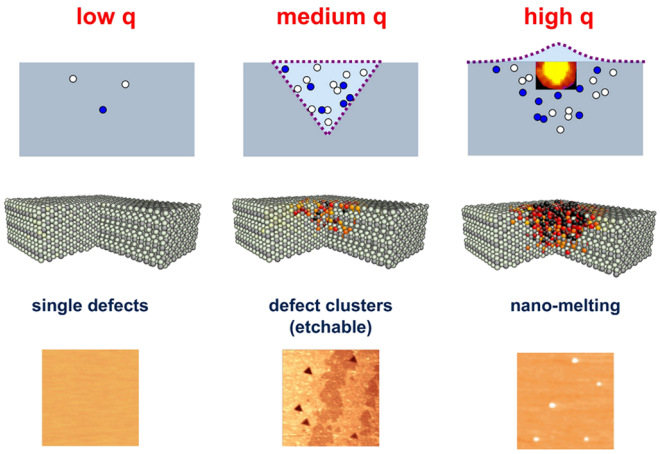

FIG. 4 (color online). Scenario for surface modification as a function of charge q or, equivalently, potential energy of the HCIs. Upper row: the charge state controls the created surface modification from nonetchable single defects (low q) to defect aggregates (medium q) and to locally molten zones (high q), schematically. Lower row: AFM images. Center row: typical results of molecular dynamics simulations showing that the initial electronic excitation of the surface and energy transfer to the lattice leads to a considerable number of displacements (center column) even before melting of the surface sets in (right column); center figures created using AtomEye [28].

For larger q and, correspondingly, larger potential energy, the sputtering yield [20] as well as the density of defects (excitons, color centers, Ca enriched regions due to F_2 formation) strongly increase. The latter is now large enough to lead to defect clusters and aggregates (Fig. 4, center column). Depending on their mobility, defects may diffuse to the surface, leading to defect-mediated desorption [21] and thus form (monoatomic) pits as observed in the case of the alkali halide KBr [11]. The defect-mediated desorption mechanism is less probable in CaF_2 since color center recombination below the surface is much more likely [22] due to the small energy gain of color center pair formation as well as the formation of more complex (and therefore immobile) defect agglomerates [23,24]. The material in the vicinity of the impact region is not ablated but structurally weakened and forms the nucleus of an etchable defect subsequently removed by a suitable etchant [15]. The synergistic effect induced by the accompanying kinetic energy originates from kinetically induced defects created in the collision cascade which enhance the trapping of the color centers created by potential energy [25] and therefore increases defect agglomeration. Consequently, the borderline between the regions A (stable) and B (etchable surface defects) has a negative slope in the phase diagram (Fig. 3). While our MD simulation cannot directly account for the defect cluster formation (due to the lack of realistic binary potentials for color centers and charge-exchanged constituents), it shows in the regime of phase B atomic displacements of the order of a few percent of the impact region, the overwhelming majority of which are fluorine atoms (Fig. 4, center). This is believed to be a necessary precursor for defect aggregation.

At still higher potential energies (Fig. 4, right column), heating of the lattice atoms by primary and secondary electrons from the deexcitation of the HCIs surpasses the melting threshold of the solid [8,18]. Heat and pressure deforms the surface and after rapid quenching a hillock remains at the surface. With increasing kinetic energy, the region where the potential energy of the HCIs is deposited, extends slightly deeper into the target [8]. Therefore, the kinetic energy dependence of the borderline between the region of nanohillock formation (region C) and defect clustering without protrusion (region B) is only weak with a slightly positive slope. The overall surface damage (lattice distortion, defect aggregations) extends well beyond the molten core. While the latter determines the diameter of the hillock, the former determines the size of the nucleus of the etch pit. Within the MD simulations a much larger number of displacements ($\sim 25\%$) is observed in region C, a significant fraction of which are calcium atoms.

Even though the present scenario is demonstrated specifically for CaF_2, we surmise that it should hold for other halide crystals as well. While borderlines between different regions A, B, and C will, of course, depend on the specific target material, we expect the phase diagram (Fig. 3) to remain qualitatively valid. For BaF_2 (111) and KBr (001), for example, we have previously observed the A and B phases [15,26]. The phase diagram predicts that by further increasing the potential energy of the HCIs we should be able to reach region C, i.e., hillock formation (or melting) in line with first indications for hillock formation on BaF_2 [27].

In summary, we have established a phase diagram for stable nanoscale surface modification of alkaline earth halides and alkali halides by highly charged ion impact with its potential and kinetic energies as control parameters. In addition to the region of predominantly potential energy driven melting and hillock formation, a second region was identified in which a sufficient number of defects agglomerate such that chemical etchants are able to remove material leaving triangular shaped pits on the surface. The etchability of the defect cluster not only depends on the potential energy of the HCIs but also strongly on the kinetic energy of the projectile. This scenario seems to be generally applicable to other alkaline earth and alkali halide surfaces as well.

A. S. E. thanks the Alexander von Humboldt Foundation for financial support. The Deutsche Forschungsgemeinschaft (DFG) is gratefully acknowledged for financial support under Project No. HE 6174/1-1. R. R. is a recipient of a DOC-fellowship of the Austrian Academy of Sciences. Support from the Austrian Science Foundation FWF under Project No. SFB-041 ViCoM and the International Max Planck Research School of Advanced Photon Science APS (G. W.) is acknowledged.

*a.s.el-said@hzdr.de
†s.facsko@hzdr.de
‡aumayr@iap.tuwien.ac.at

[1] A. Arnau, F. Aumayr, P. M. Echenique, M. Grether, W. Heiland, J. Limburg, R. Morgenstern, P. Roncin, S. Schippers, R. Schuch, N. Stolterfoht, P. Varga, T. J. M. Zouros, and H. P. Winter, Surf. Sci. Rep. **27**, 113 (1997).
[2] A. V. Hamza, M. W. Newman, P. A. Thielen, H. W. H. Lee, T. Schenkel, J. W. McDonald, and D. H. Schneider, Appl. Phys. Lett. **79**, 2973 (2001).
[3] M. Tona, H. Watanabe, S. Takahashi, N. Nakamura, N. Yoshiyasu, M. Sakurai, T. Terui, S. Mashiko, C. Yamada, and S. Ohtani, Nucl. Instrum. Methods Phys. Res., Sect. B **256**, 543 (2007).
[4] J. M. Pomeroy, H. Grube, A. C. Perrella, and J. Gillaspy, Appl. Phys. Lett. **91**, 073506 (2007).
[5] R. E. Lake, J. M. Pomeroy, H. Grube, and C. E. Sosolik, Phys. Rev. Lett. **107**, 063202 (2011).
[6] A. V. Hamza, T. Schenkel, A. V. Barnes, and D. H. Schneider, J. Vac. Sci. Technol. A **17**, 303 (1999).
[7] M. Tona, S. Takahashi, K. Nagata, N. Yoshiyasu, C. Yamada, N. Nakamura, S. Ohtani, and M. Sakurai, Appl. Phys. Lett. **87**, 224102 (2005).
[8] A. S. El-Said, R. Heller, W. Meissl, R. Ritter, S. Facsko, C. Lemell, B. Solleder, I. C. Gebeshuber, G. Betz, M. Toulemonde, W. Möller, J. Burgdörfer, and F. Aumayr, Phys. Rev. Lett. **100**, 237601 (2008).
[9] M. Tona, H. Watanabe, S. Takahashi, N. Nakamura, N. Yoshiyasu, M. Sakurai, T. Terui, S. Mashiko, C. Yamada, and S. Ohtani, Surf. Sci. **601**, 723 (2007).
[10] M. Tona, Y. Fujita, C. Yamada, and S. Ohtani, Phys. Rev. B **77**, 155427 (2008).
[11] R. Heller, S. Facsko, R. A. Wilhelm, and W. Möller, Phys. Rev. Lett. **101**, 096102 (2008).
[12] F. Aumayr, S. Facsko, A. S. El-Said, C. Trautmann, and M. Schleberger, J. Phys. Condens. Matter **23**, 393001 (2011).
[13] C. Motzer and M. Reichling, J. Appl. Phys. **105**, 064309 (2009).
[14] I. Horcas, R. Fernandez, J. M. Gomez-Rodriguez, J. Colchero, J. Gomez-Herrero, and A. M. Baro, Rev. Sci. Instrum. **78**, 013705 (2007).
[15] A. S. El-Said, R. Heller, F. Aumayr, and S. Facsko, Phys. Rev. B **82**, 033403 (2010).
[16] J. Burgdörfer, P. Lerner, and F. W. Meyer, Phys. Rev. A **44**, 5674 (1991).
[17] B. Solleder, C. Lemell, K. Tökesi, N. Hatcher, and J. Burgdörfer, Phys. Rev. B **76**, 075115 (2007).
[18] G. Wachter, Diplom thesis, TU Wien-Vienna University of Technology, 2009 (unpublished), http://www.ub.tuwien.ac.at/dipl/2009/AC07452619.pdf.
[19] C. Trautmann, K. Schwartz, and O. Geiss, J. Appl. Phys. **83**, 3560 (1998).
[20] F. Aumayr and H. P. Winter, Phil. Trans. R. Soc. A **362**, 77 (2004).
[21] G. Hayderer, M. Schmid, P. Varga, H. Winter, F. Aumayr, L. Wirtz, C. Lemell, J. Burgdörfer, L. Hagg, and C. O. Reinhold, Phys. Rev. Lett. **83**, 3948 (1999).
[22] R. T. Williams, Radiat. Eff. Defects Solids **109**, 175 (1989).
[23] S. Rix, U. Natura, M. Letz, C. Felser, and L. Parthier, Proc. SPIE Int. Soc. Opt. Eng. **7504**, 75040J (2009).
[24] S. Rix, Ph.D. thesis, Johannes Gutenberg-University Mainz, 2011 (unpublished).
[25] G. Hayderer, S. Cernusca, M. Schmid, P. Varga, H. P. Winter, F. Aumayr, D. Niemann, V. Hoffmann, N. Stolterfoht, C. Lemell, L. Wirtz, and J. Burgdörfer, Phys. Rev. Lett. **86**, 3530 (2001).
[26] S. Facsko, R. Heller, A. S. El-Said, W. Meissl, and F. Aumayr, J. Phys. Condens. Matter **21**, 224012 (2009).
[27] A. S. El-Said, R. Heller, and S. Facsko, Nucl. Instrum. Methods Phys. Res., Sect. B **269**, 901 (2011).
[28] J. Li, Model. Simulat. Mater. Sci. Eng. **11**, 173 (2003).